Highly Porous Fe/N/C Catalyst for Oxygen Reduction: The Importance of Pores

Experimental Section

Synthesis of g-C_3N_4

Urea loaded in a covered corundum crucible was heated in a muffle furnace to desired temperature (525, 550, 575 and 600) with a heating rate of 5 °C min^{-1} and kept at that temperature for 4 h. The obtained g-C_3N_4 sample was denoted as g-C_3N_4-T (T represents pyrolysis temperature).

Synthesis of Fe/N/C

0.5 g of g-C_3N_4, 2 g of glucose and 30 mg of $FeCl_3 \cdot 6H_2O$ were added to 40 mL of H_2O, and the resultant suspension was ultrasonicated for 4 h and then transferred to a 50-mL Teflon-lined autoclave, which was then placed in a convection oven and kept at 160 °C for 10 h. The resultant product was centrifuged and washed alternately with ethanol and deionized water, and after three-time centrifugation-washing cycles the obtained sample was dried at 80 °C overnight and then transferred to a covered corundum boat placed in a quartz tube furnace, which was heated to 1100 °C with a heating rate of 5 °C min^{-1} and kept at that temperature for 1 h under flowing N_2. The finally obtained sample was denoted as Fe/N/C-T (T represents the pyrolysis temperature of g-C_3N_4 obtained).

Material characterization

The morphology, structure and composition of the synthesized materials were characterized by transmission electron microscopy (TEM, JEM-2100, JEOL), high-resolution TEM (HRTEM, Titan Themis 200, FEI) equipped with energy-dispersive X-ray spectrometry (EDS, Super-X, Bruker), X-ray diffraction (XRD, D8 Advance, Bruker), X-ray photoelectron spectroscopy (XPS, VG Multilab 2000, Bruker), surface area and porosity analyzer (ASAP2460, Micromeritics), Inductively coupled plasma mass spectrometry (ICP-

MS, 7700, Agilent Technology) and laser confocal micro-Raman spectroscopy (DXR, American Thermo Electron).

Electrochemical characterization

Electrochemical measurements were carried out by using an electrochemical workstation (PGSTAT 302 N, Metrohm Autolab) in a three-electrode system consisting of a graphite rod counter electrode, a Hg/HgO reference electrode, and a catalyst-modified glassy-carbon (GC) working electrode (3 mm in diameter). All the electrode potentials reported in this work were reported with respect to reversible hydrogen electrode (RHE). The loading of Fe/N/C sample on the GC electrode was 397 $\mu g \cdot cm^{-2}$ and the loading of the commercial Pt/C (20 wt. %, Johnson Matthey) catalyst on GC electrode was 132 $\mu g \cdot cm^{-2}$. The electrolyte was 0.1 M KOH solution, and its temperature was maintained at 25 °C with circulating ethylene glycol/water. The ORR performance of the catalyst was measured in O_2-saturated 0.1 M KOH solution by linear sweep voltammetry (LSV) with a sweep rate of 10 mV s^{-1} at 1600 rpm. Rotating ring-disk electrode (RRDE, Pine) was used to determine the HO_2^- yield and the electron transfer number (n) with the Pt ring potential set to 1.2 V vs. RHE. The HO_2^- yield and the electron transfer number during the ORR process were determined based on the following equations [1],

$$\mathrm{HO_2^-}(\%) = 200\frac{I_\mathrm{r}/\mathrm{N}}{I_\mathrm{d}+I_\mathrm{r}/\mathrm{N}} \quad (1)$$

$$n=4\frac{I_\mathrm{d}}{I_\mathrm{d}+I_\mathrm{r}/\mathrm{N}} \quad (2)$$

where I_r is the ring current, I_d is the disk current, and N is the collecting efficiency of Pt ring (0.37).

DFT calculation

Cambridge Sequential Total Energy Package (CASTEP) code was used for DFT calculations. The

valence-core interaction was described by using a ultrasoft pseudopotential approach and an energy cutoff of 600 eV was used for plane-wave expansion. The exchange-correlation functional was described by Perdew-Burke-Ernzerhof (PBE) functional with the generalized gradient approximation (GGA). The single-layer g-C_3N_4 (001) slab was constructed with a 2 × 2 supercell, two-layer Pt (111) slabs were constructed, and a single-layer Fe/N/C slab was constructed with an 8 × 6 supercell, all with a vacuum region of 15 Å to avoid interaction between slabs. The convergence criteria for energy and force were set as 0.00001 eV and 0.01 eV/Å, respectively. The energy difference between the g-C_3N_4-coordinated Fe system and the corresponding isolated systems, were calculated based on Equation 3,

$$\Delta E_{\text{adsorption}} = E_{\text{Fe/g-C}_3\text{N}_4} - E_{\text{Fe}} - E_{\text{g-C}_3\text{N}_4} \qquad (3)$$

where $\Delta E_{\text{adsorption}}$ was the adsorption energy of Fe^{3+} ion or Fe atom at the "nitrogen pot" of g-C_3N_4, and $E_{\text{Fe/g-C}_3\text{N}_4}$, E_{Fe} and $E_{\text{g-C}_3\text{N}_4}$ were the total energies of the g-C_3N_4-coordinated Fe system, single Fe^{3+} ion or Fe atom, and bare g-C_3N_4, respectively.

The Gibbs free energy change (ΔG) corresponding to each reaction was determined through $\Delta G = \Delta E + \Delta\text{ZPE} - T\Delta S$, where ΔE, ΔZPE and ΔS were the changes in energy, in zero-point energies, and in entropy, respectively, and T was the temperature (298.15 K). The Gibbs free energy of $H_2O(l)$ was calculated from the ideal gas of $H_2O(g)$ by $G_{\text{H}_2\text{O(l)}} = G_{\text{H}_2\text{O(g)}} + RT\ln(p/p_0)$, where R was the ideal gas constant, T was 298.15 K, and P and P_0 were 0.035 and 1 bar, respectively. The Gibbs free energy of O_2 was derived as $G_{\text{O}_2} = 2G_{\text{H}_2\text{O(l)}} - 2G_{\text{H}_2} + 4.92$ and that of OH^- was derived as $G_{\text{OH}^-} = G_{\text{H}_2\text{O(l)}} - G_{\text{H}^+} = G_{\text{H}_2\text{O(l)}} - 1/2G_{\text{H}_2}$ [2]. The electrode potential effect on G was adjusted by shifting the

G at zero potential by neU, where U and n were the electrode potential vs. RHE and the number of electrons transferred, respectively [3].

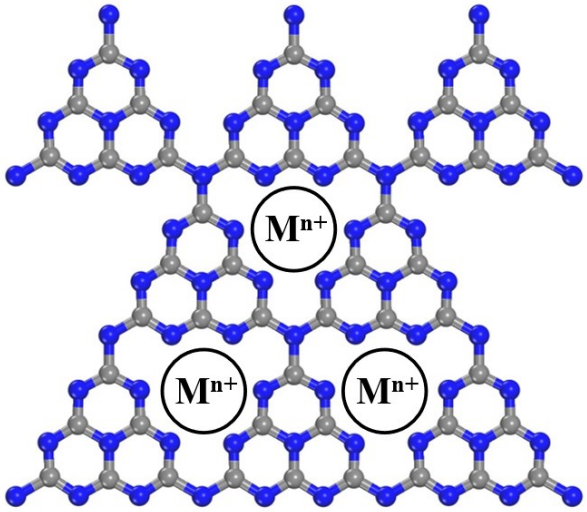

Fig. S1. Schematic illustration of the g-C_3N_4 framework with the inclusion of metal ion (M^{n+}) via an ion coordination route.

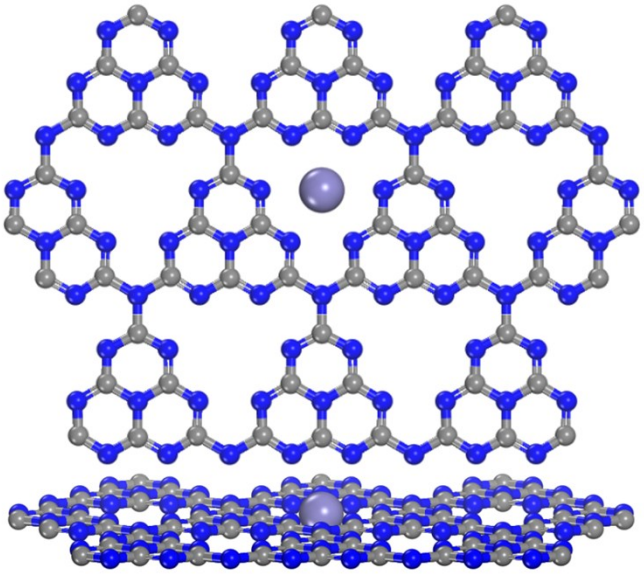

Fig. S2. Stable configurations of Fe^{3+} ion and Fe atom in the nitrogen pore.

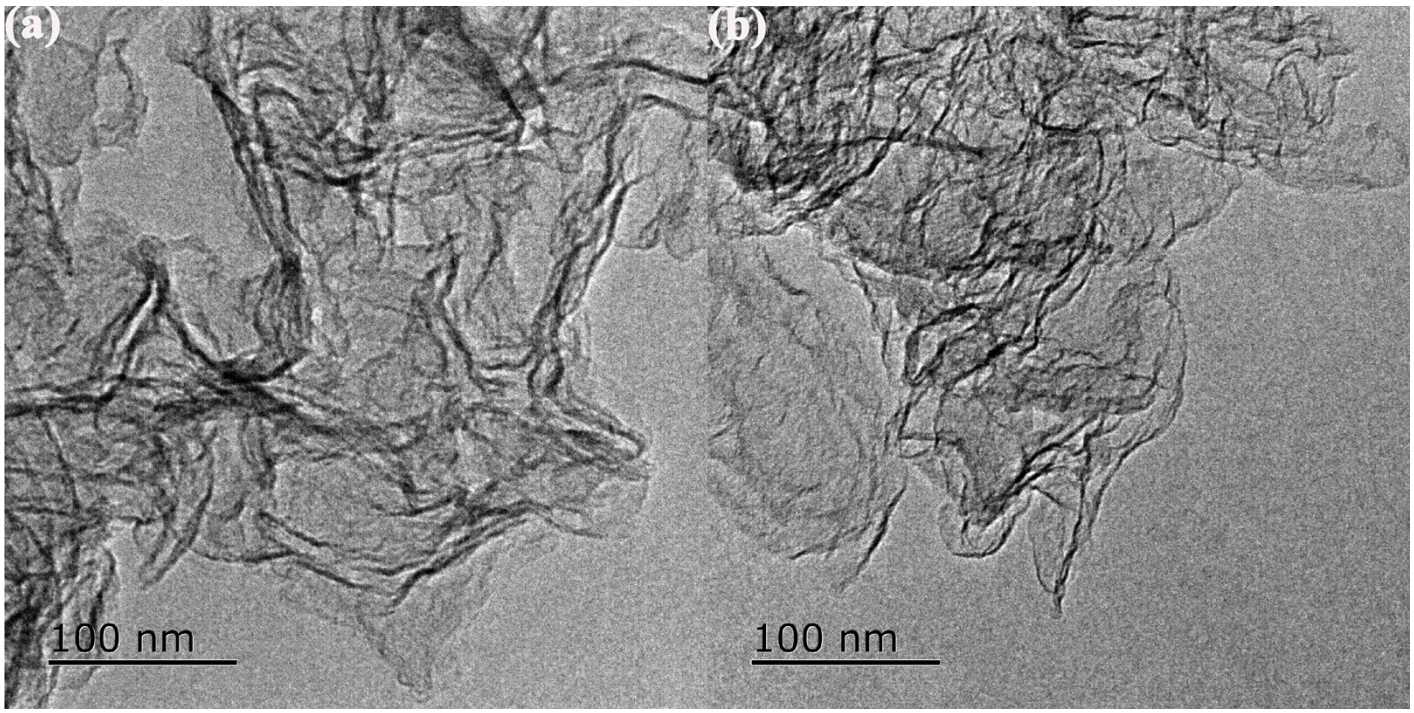

Fig. S3. TEM images of Fe/N/C-525 (a) and Fe/N/C-550 (b).

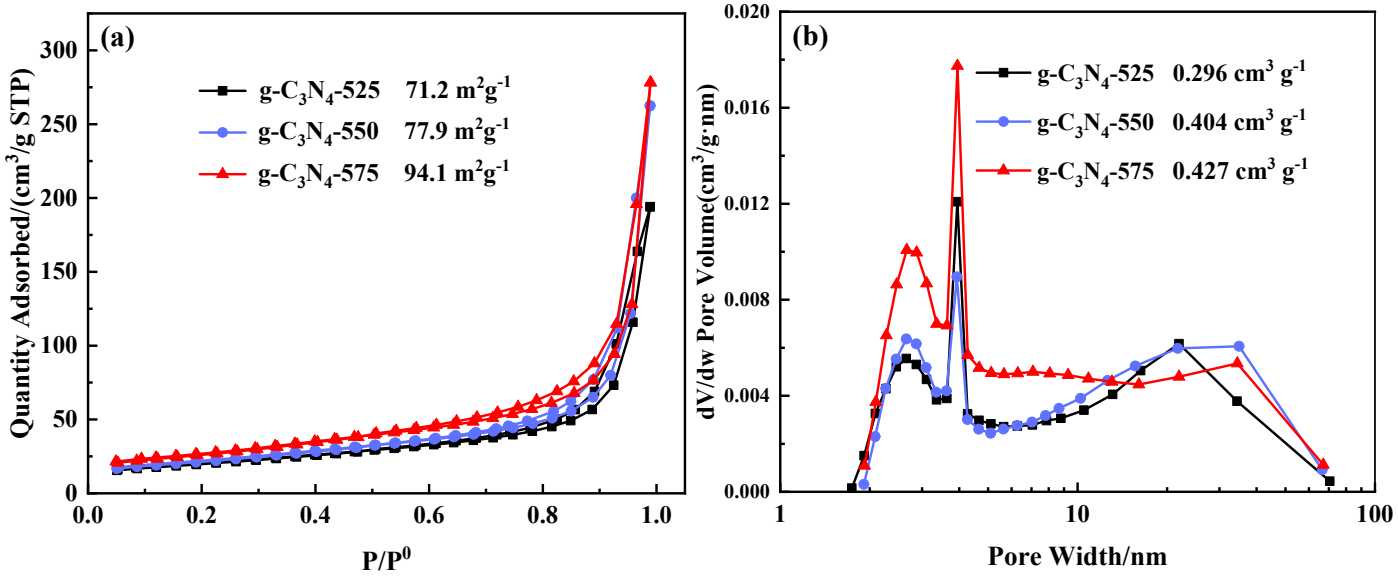

Fig. S4. N_2 adsorption-desorption isotherms (a) and the corresponding pore distribution curves (b) of g-C_3N_4 samples.

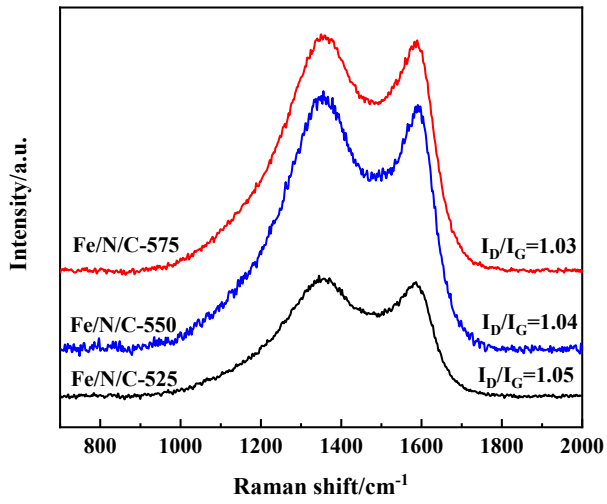

Fig. S5. Raman spectra of Fe/N/C samples.

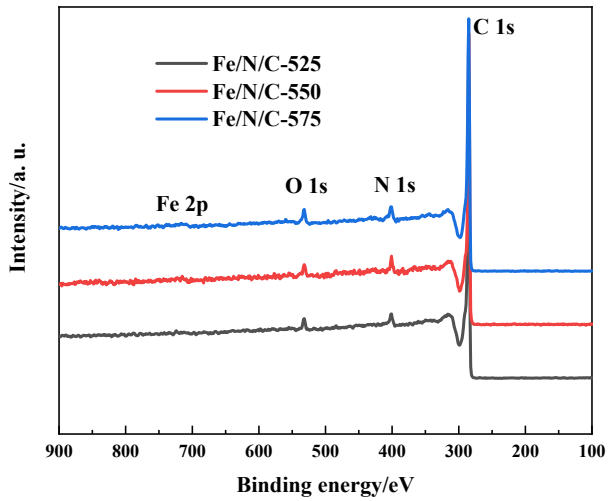

Fig. S6. XPS spectra of Fe/N/C samples.

Table S1. Compositions of Fe/N/C samples determined by XPS and ICP-MS.

Sample	C/at. %	O/at. %	Fe/at. %	N/at. %	Fe/wt. % *
Fe/N/C-525	94.61	2.00	0.29	3.61	1.23
Fe/N/C-550	92.95	2.52	0.40	4.12	1.75
Fe/N/C-575	92.88	2.50	0.34	4.28	1.50

* Fe content determined by ICP-MS.

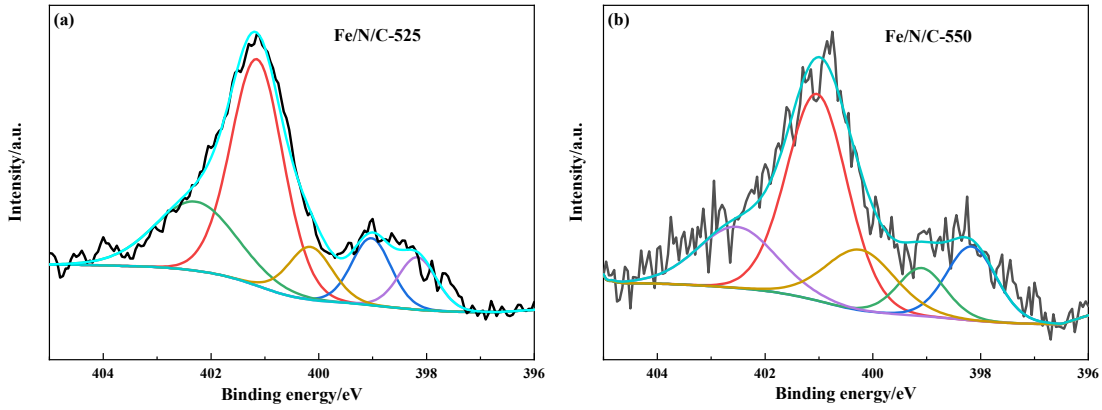

Fig. S7. High-resolution N1s spectra of Fe/N/C-525 and Fe/N/C-550.

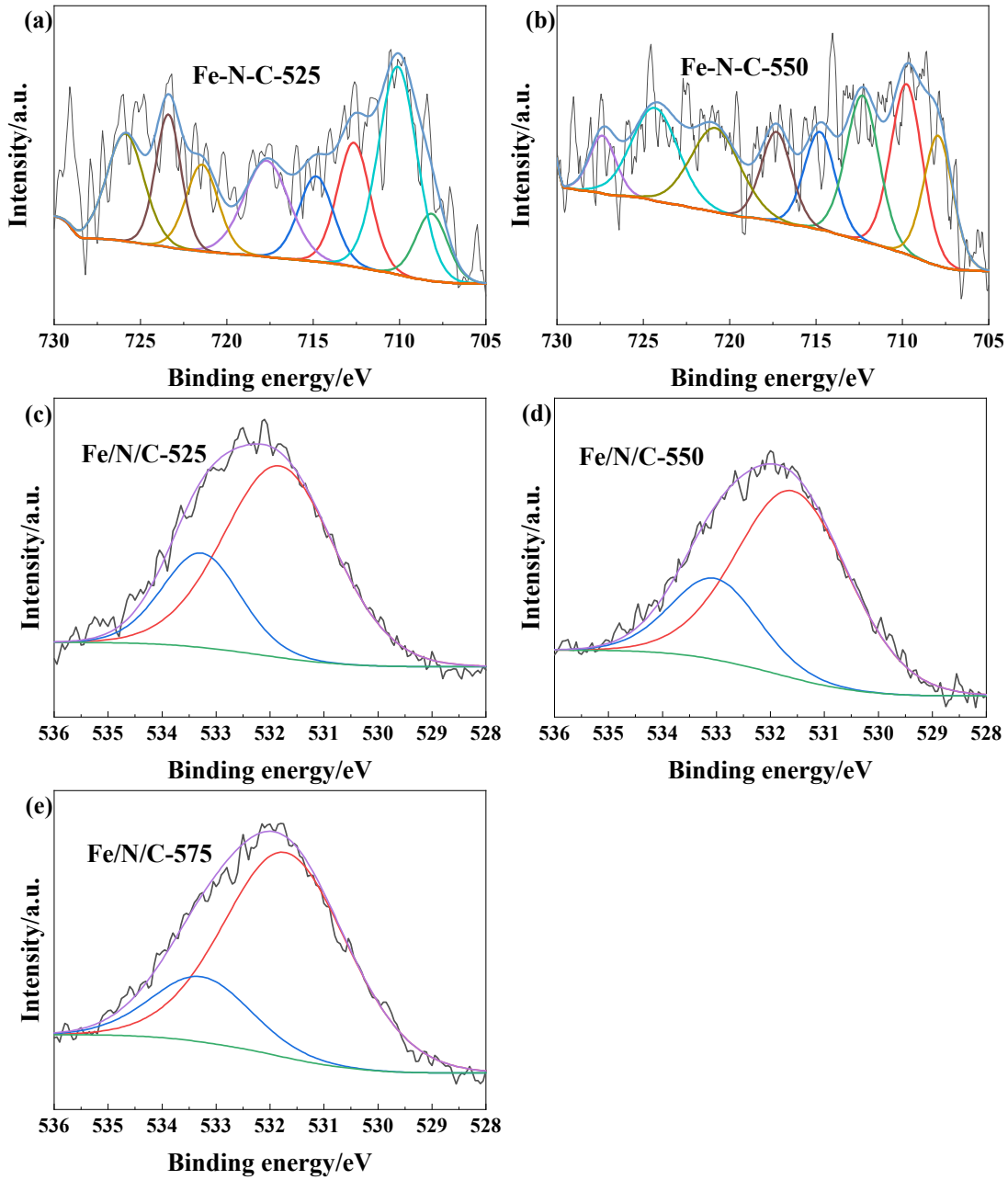

Fig. S8. Fe 2p spectra of Fe/N/C-525 (a) and Fe/N/C-550 (b), O 1s spectra of Fe/N/C-525 (c), Fe/N/C-550 (d), and Fe/N/C-575 (e).

Table S2. ORR activity of Fe/N/C and Pt/C catalysts.

Sample	E_{onset}/V	$E_{1/2}$/V	j_k/mA cm^{-2}@0.9 V	j_m/mA mg^{-1}@0.9 V
Fe/N/C-525	0.938	0.851	0.768	1.935
Fe/N/C-550	0.962	0.868	1.692	4.262
Fe/N/C-575	0.966	0.882	2.481	6.246
Pt/C	0.956	0.851	1.237	9.371
Fe/N/C-575-A	0.972	0.890	3.614	9.103

j_m=mass specific activity

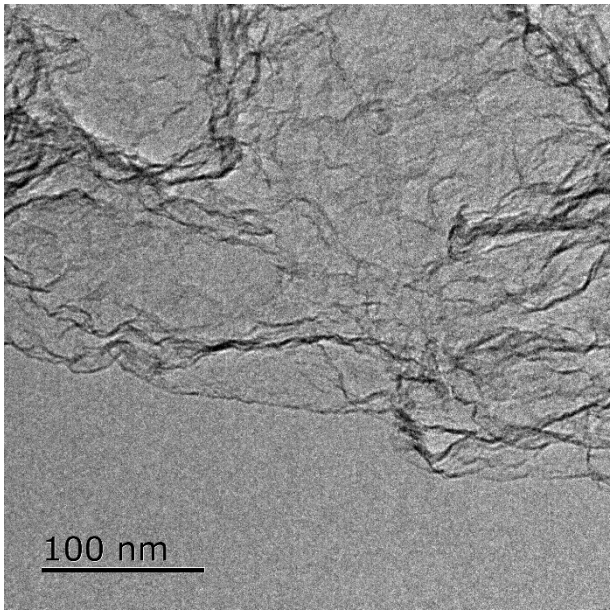

Fig. S9. TEM image of Fe/N/C-575-A sample.

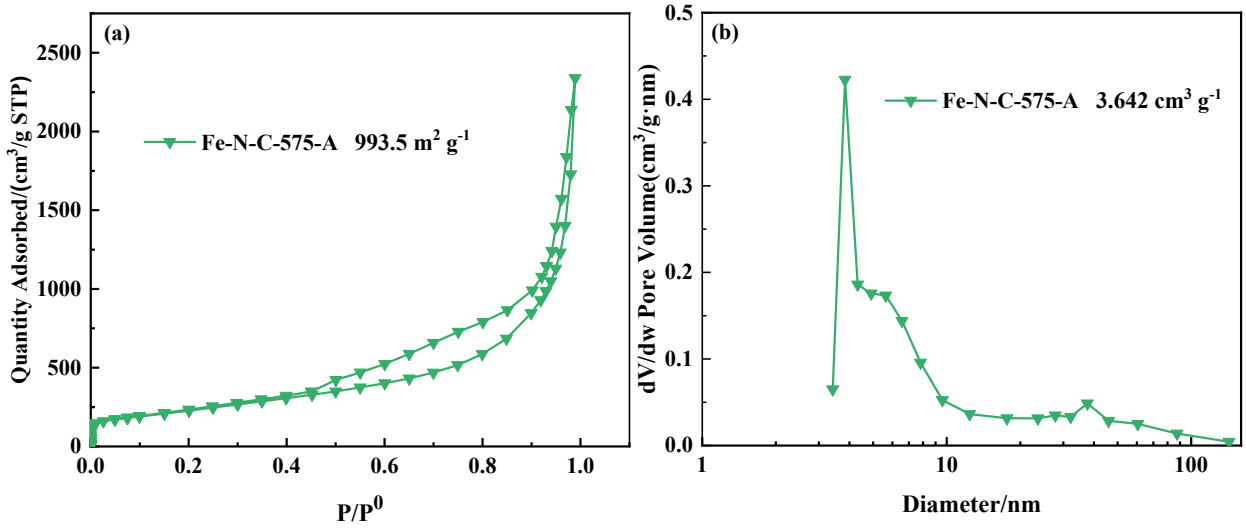

Fig. S10. N_2 adsorption-desorption isotherm (a) and the corresponding pore distribution curve (b) of Fe/N/C-575-A sample.

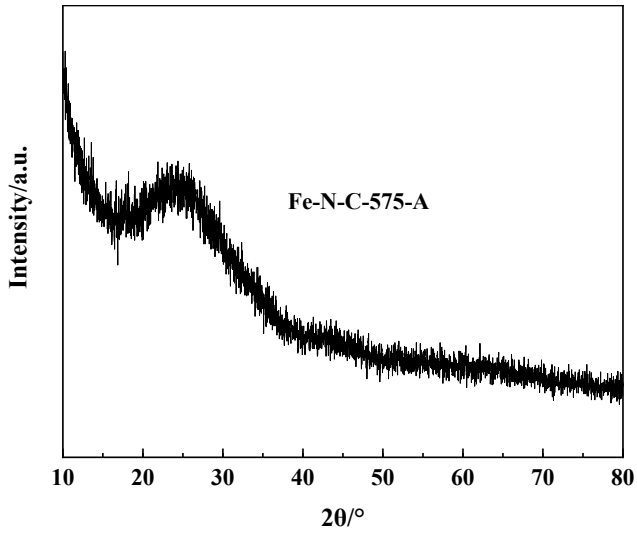

Fig. S11. XRD pattern of Fe/N/C-575-A sample.

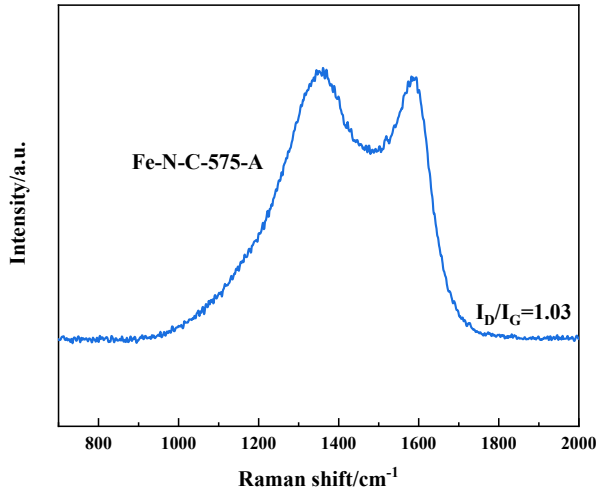

Fig. S12. Raman spectrum of Fe/N/C-575-A sample.

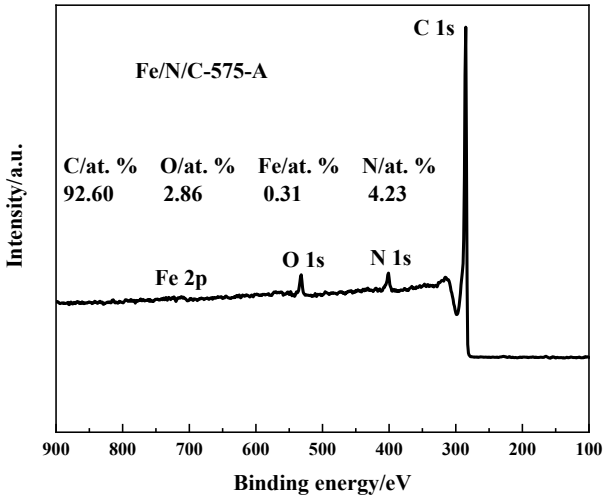

Fig. S13. XPS spectrum of Fe/N/C-575-A sample.

The associated mechanism of ORR in alkaline environment was as follows [4, 5],

$O_2 + * \rightarrow O_2*$ (4)

$O_2* + H_2O + e^- \rightarrow OOH* + OH^-$ (5)

$OOH* + e^- \rightarrow O* + OH^-$ (6)

$O* + H_2O + e^- \rightarrow OH* + OH^-$ (7)

$OH* + e^- \rightarrow OH^- + *$ (8)

where * denoted the active site in catalyst.

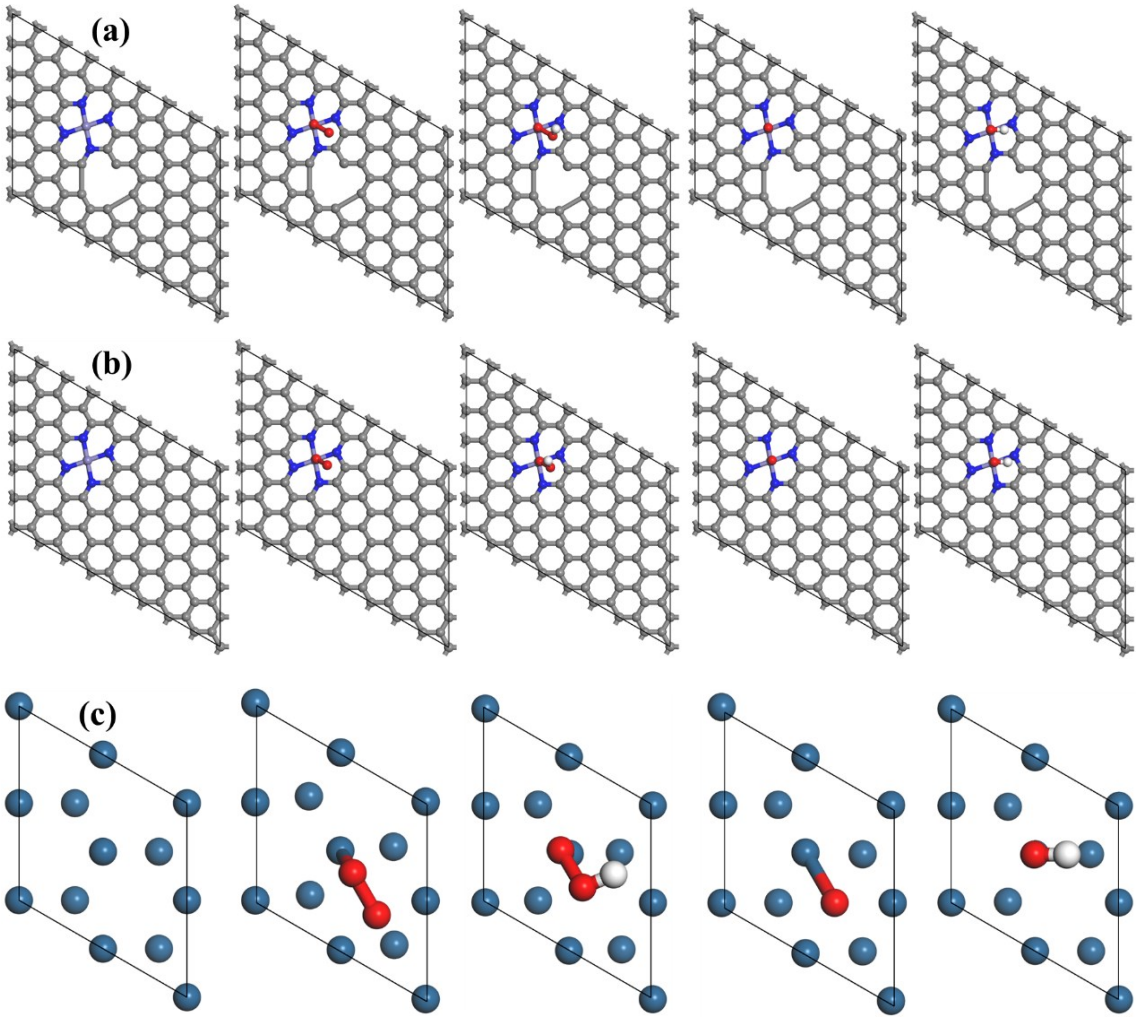

Fig. S14. Stable configurations of four oxygen-containing species O_2, OOH, O and OH adsorbed on Fe-N_4 with (a) and without (b) adjacent pore and on Pt (111) (c) (the gray, blue, purple, red and white balls represent C, N, Fe, O and H atoms, respectively).

Table S3. Comparison of ORR performance of non-precious catalyst.

Catalyst	E_{onset} [V]	$E_{1/2}$ [V]	Reference
Fe/N/C-575-A	1.032	0.908	This work
FeN_x-embedded PNC	0.997	0.86	6
Fe-NC SAC	0.98	0.90	7
FeNC-1	/	0.90	8
Fe-ISA/SNC	/	0.896	9
Co/Co-N-C	0.97	0.85	10
Cu@Fe-N-C	1.01	0.892	11
Fe-N-C HNSs	1.045	0.87	12
Co-N-C/CoO_x-800	0.89	0.82	13
Cu-Fe-N-C	0.967	0.864	14
Zn/CoN-C	1.004	0.861	15
Fe/Fe_5C_2@N-C-1000	/	0.85	16
SA-Fe-HPC	/	0.89	17
FeSAs/PTF-600	1.01	0.87	18
CoN_4/NG	0.98	0.87	19
1100-CNS	0.99	0.85	20
N-Fe/CNs-700-800-NH_3	0.930	0.859	21
S, N-Fe/N/C-CNT	/	0.85	22
FeBNC	0.968	0.838	23
SA-Fe/NG	/	0.88	24
3D MPC	/	0.88	25

The methanol crossover effect on the catalytic performance of catalyst was examined by chronoamperometric test, which was carried out in O_2-saturated 0.1 M KOH solution at 0.625 V vs. RHE and 1600 rpm.

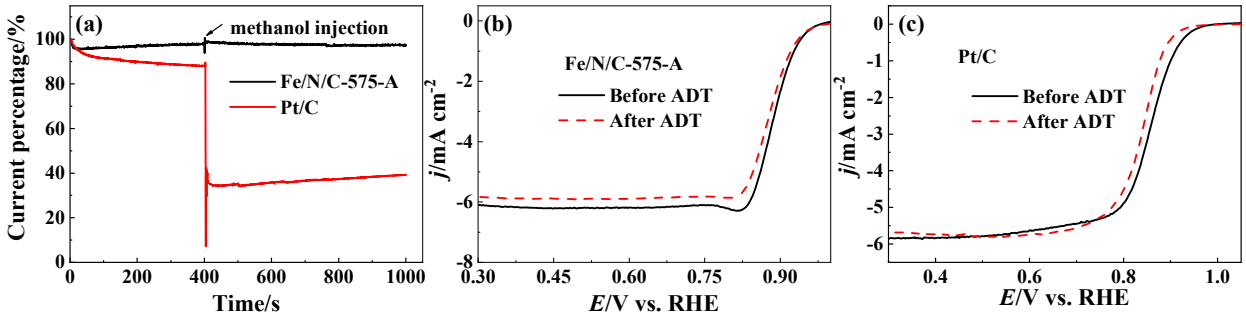

Fig. S15. Chronoamperometric responses of Fe/N/C-575-A and Pt/C catalysts (a), LSV curves of Fe/N/C-575-A (b) and Pt/C (c) before and after ADT.

References

1. H. Zhao, C.-C. Weng, J.-T. Ren, L. Ge, Y.-P. Liu and Z.-Y. Yuan, *Chinese J. Catal.*, 2020, **41**, 259-267.

2. J. K. Nørskov, J. Rossmeisl, A. Logadottir, L. Lindqvist, J. R. Kitchin, T. Bligaard and H. Jónsson, *J. Phys. Chem. B*, 2004, **108**, 17886-17892.
3. K. Liu, Z. Qiao, S. Hwang, Z. Liu, H. Zhang, D. Su, H. Xu, G. Wu and G. Wang, *Appl. Catal. B-Environ.*, 2019, **243**, 195-203.
4. F. Li, G.-F. Han, H.-J. Noh, S.-J. Kim, Y. Lu, H. Y. Jeong, Z. Fu and J.-B. Baek, *Energ. Environ. Sci.*, 2018, **11**, 2263-2269.
5. X. Xiong, Y. Li, Y. Jia, Y. Meng, K. Sun, L. Zheng, G. Zhang, Y. Li and X. Sun, *Nanoscale*, 2019, **11**, 15900-15906.
6. L. Ma, S. Chen, Z. Pei, Y. Huang, G. Liang, F. Mo, Q. Yang, J. Su, Y. Gao, J. A. Zapien and C. Zhi, *ACS Nano*, 2018, **12**, 1949-1958.
7. L. Zhao, Y. Zhang, L.-B. Huang, X.-Z. Liu, Q.-H. Zhang, C. He, Z.-Y. Wu, L.-J. Zhang, J. Wu, W. Yang, L. Gu, J.-S. Hu and L.-J. Wan, *Nat. Commun.*, 2019, **10**, 1278-1288.
8. W. Wang, M. Tang, Z. Zheng and S. Chen, *Adv. Energy Mater.*, 2019, **9**, 1803628.
9. Q. Li, W. Chen, H. Xiao, Y. Gong, Z. Li, L. Zheng, X. Zheng, W. Yan, W.-C. Cheong, R. Shen, N. Fu, L. Gu, Z. Zhuang, C. Chen, D. Wang, Q. Peng, J. Li and Y. Li, *Adv. Mater.*, 2018, **30**, 1800588.
10. S. Wang, Q. He, C. Wang, H. Jiang, C. Wu, S. Chen, G. Zhang and L. Song, *Small*, 2018, **14**, 1800128.
11. Z. Wang, H. Jin, T. Meng, K. Liao, W. Meng, J. Yang, D. He, Y. Xiong and S. Mu, *Adv. Funct. Mater.*, 2018, **28**, 1802596.
12. Y. Chen, Z. Li, Y. Zhu, D. Sun, X. Liu, L. Xu and Y. Tang, *Adv. Mater.*, 2019, **31**, 1806312.
13. X. Guo, C. Qian, R. Shi, W. Zhang, F. Xu, S. Qian, J. Zhang, H. Yang, A. Yuan and T. Fan, *Small*, 2019, **15**, 1804855.
14. J. Li, J. Chen, H. Wan, J. Xiao, Y. Tang, M. Liu and H. Wang, *Appl. Catal. B-Environ.*, 2019, **242**, 209-217.
15. Z. Lu, B. Wang, Y. Hu, W. Liu, Y. Zhao, R. Yang, Z. Li, J. Luo, B. Chi, Z. Jiang, M. Li, S. Mu, S. Liao, J. Zhang and X. Sun, *Angew. Chem. Int. Ed.*, 2019, **131**, 2648-2652.
16. L. Song, T. Wang, L. Li, C. Wu and J. He, *Appl. Catal. B-Environ.*, 2019, **244**, 197-205.
17. Z. Zhang, J. Sun, F. Wang and L. Dai, *Angew. Chem. Int. Ed.*, 2018, **130**, 9176-9181.
18. J.-D. Yi, R. Xu, Q. Wu, T. Zhang, K.-T. Zang, J. Luo, Y.-L. Liang, Y.-B. Huang and R. Cao, *ACS Energy Lett.*, 2018, **3**, 883-889.
19. L. Yang, L. Shi, D. Wang, Y. Lv and D. Cao, *Nano Energy*, 2018, **50**, 691-698.
20. Z. Pei, H. Li, Y. Huang, Q. Xue, Y. Huang, M. Zhu, Z. Wang and C. Zhi, *Energ. Environ. Sci.*, 2017, **10**, 742-749.
21. S. Li, C. Cheng, H.-W. Liang, X. Feng and A. Thomas, *Adv. Mater.*, 2017, **29**, 1700707.
22. P. Chen, T. Zhou, L. Xing, K. Xu, Y. Tong, H. Xie, L. Zhang, W. Yan, W. Chu, C. Wu and Y. Xie, *Angew. Chem. Int. Ed.*, 2017, **56**, 610-614.
23. K. Yuan, S. Sfaelou, M. Qiu, D. Lützenkirchen-Hecht, X. Zhuang, Y. Chen, C. Yuan, X. Feng and U. Scherf, *ACS Energy Lett.*, 2018, **3**, 252-260.
24. L. Yang, D. Cheng, H. Xu, X. Zeng, X. Wan, J. Shui, Z. Xiang and D. Cao, *Proc. Natl. Acad. Sci. USA*, 2018, **115**, 6626-6631.
25. W. Wang, W. Chen, P. Miao, J. Luo, Z. Wei and S. Chen, *ACS Catal.*, 2017, **7**, 6144-6149.